A Common Catalytic Mechanism for Proteins of the HutI Family†

Rajiv Tyagi,‡ Subramaniam Eswaramoorthy,‡ Stephen K. Burley,§ Frank M. Raushel,|| and Subramanyam Swaminathan*,‡

Biology Department, Brookhaven National Laboratory, Upton, New York 11973, SGX Pharmaceuticals, Inc., San Diego, California 92121, and Department of Chemistry, P.O. Box 30012, Texas A&M University, College Station, Texas 77842-3012

Received January 31, 2008; Revised Manuscript Received March 24, 2008

ABSTRACT: Imidazolonepropionase (HutI) (imidazolone-5-propanote hydrolase, EC 3.5.2.7) is a member of the amidohydrolase superfamily and catalyzes the conversion of imidazolone-5-propanoate to *N*-formimino-L-glutamate in the histidine degradation pathway. We have determined the three-dimensional crystal structures of HutI from *Agrobacterium tumefaciens* (At-HutI) and an environmental sample from the Sargasso Sea Ocean Going Survey (Es-HutI) bound to the product [*N*-formimino-L-glutamate (NIG)] and an inhibitor [3-(2,5-dioxoimidazolidin-4-yl)propionic acid (DIP)], respectively. In both structures, the active site is contained within each monomer, and its organization displays the landmark feature of the amidohydrolase superfamily, showing a metal ligand (iron), four histidines, and one aspartic acid. A catalytic mechanism involving His265 is proposed on the basis of the inhibitor-bound structure. This mechanism is applicable to all HutI forms.

In certain eubacteria, such as *Agrobacterium tumefaciens* and *Pseudomonas aeruginosa,* L-histidine can be metabolized to L-glutamate via catalytic transformation by five enzymes (*1*). In the first step, L-histidine is deaminated by histidine ammonia lyase (HutH)[1] to form urocanate, which is subsequently hydrated in a mechanistically complex reaction by urocanase (HutU) to produce imidazolone-5-propionate. This product is in turn hydrolyzed by imidazolonepropionase (HutI) to generate *N*-formimino-L-glutamate. The *N*-formimino substituent is then hydrolyzed by *N*-formimino-L-glutamate deiminase (HutF) to form *N*-formyl-L-glutamate and ammonia. In the final step, *N*-formyl-L-glutamate amidohydrolase (HutG) catalyzes hydrolysis of *N*-formyl-L-glutamate to L-glutamate and formate. In some organisms, the *N*-formimino-L-glutamate is hydrolyzed directly to formamide and L-glutamate, and in others, the formimino group is transferred to tetrahydrofolate (*2*). The pathway for the degradation of histidine is summarized in Figure 1.

To date, four of seven enzymes comprising the histidine utilization pathway have been structurally characterized. HutH from *Pseudomonas putida* (PDB entry 1XFL) contains an unusual 4-methylideneimidazol-5-one cofactor formed by post-translational rearrangement of the -Ala-Ser-Gly- amino acid segment within this enzyme (*3*). In the active site of HutU from *P. putida*, there is a tightly bound NAD^+ that is utilized as an unusual nonredox electrophilic cofactor for hydration of urocanate (PDB entry 1UWK) (*4*). Its mechanism of action has been elucidated by biochemical methods (*5, 6*). One of three enzyme variants that can act upon the product of the HutI reaction, *N*-formimino-L-glutamate hydrolase, has been crystallized and its structure determined to high resolution (PDB entry 1XFK). More recently, the structures of HutI from *Bacillus subtilis* (PDB entry 2G3F), *A. tumefaciens* (PDB entry 2GOK), and an environmental sample from the Sargasso Sea (PDB entry 2OOF) have been determined (*7, 8*). These structures of HutI have demonstrated that it is a member of the amidohydrolase superfamily (AHS).

The AHS superfamily was first recognized by Sander and Holm on the basis of the structural and mechanistic similarities among adenosine deaminase, phosphotriesterase, and urease (*9*). All enzymes comprising this superfamily adopt a $(\beta/\alpha)_8$-barrel structural fold with an active site located at the C-terminus of the β-barrel, and all structurally characterized superfamily members possess mono- or binuclear metal centers within their active sites (*10*). Nearly all functionally characterized AHS members catalyze hydrolysis of C−O, C−N, or P−O bonds within esters, amides, or aromatic amines via activation of water or hydroxide by the metal center. However, members of this superfamily also catalyze decarboxylation reactions, addition of water to activated double bonds, and isomerization of aldose and ketose sugars (*10*). Well-characterized members of this superfamily include

† Research was supported by a National Institutes of Health Cooperative Agreement award to SGX Pharmaceuticals, Inc. (GM074945; Principal Investigator, S.K.B.) under DOE Prime Contract DEAC02-98CH10886 with Brookhaven National Laboratory. F.M.R. was supported by Grant GM071790. Financial support for X12C beamline (National Synchrotron Light Source) comes principally from the Offices of Biological and Environmental Research and of Basic Energy Sciences of the U.S. Department of Energy, and from the National Center for Research Resources of the National Institutes of Health.

* To whom correspondence should be addressed. E-mail: swami@bnl.gov. Phone: (631) 344-3187. Fax: (631) 344-3407.

‡ Brookhaven National Laboratory.

§ SGX Pharmaceuticals, Inc.

|| Texas A&M University.

[1] Abbreviations: HutI, imidazolonepropionase; HutH, histidine ammonia lyase; HutU, urocanase; NIG, *N*-formimino-L-glutamate; DIP, 3-(2,5-dioxoimidazolidin-4-yl)propionic acid; *At*, *Agrobacterium tumefaciens*; AHS, amidohydrolase superfamily; ES, Sargasso Sea Ocean Going Survey.

10.1021/bi800180g CCC: $40.75
Published on Web 04/29/2008

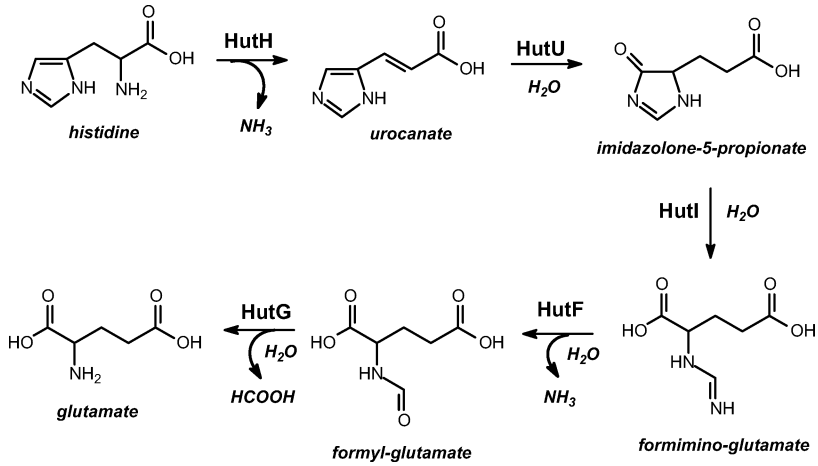

FIGURE 1: Histidine degradation pathway.

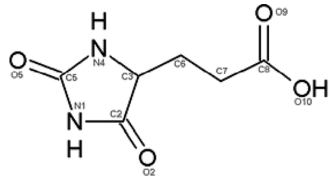

FIGURE 2: 3-(2,5-Dioxoimidazolidin-4-yl)propionic acid (DIP) inhibitor of HutI.

cytosine deaminase (*11*), dihydroorotase (*12*), isoaspartyl dipeptidase (*13*), *N*-formimino-L-glutamate deiminase (*14*), *N*-acetyl-D-glucosamine-6-phosphate deacetylase (*15*), and uronate isomerase (*16*).

The three-dimensional X-ray structures of HutI from *B. subtilis*, *A. tumefaciens*, and an environmental sample demonstrate that this enzyme has a single metal ion bound to the α-site. Most of the enzymes in the AHS with an α-mononuclear metal center catalyze the deamination of an aromatic amine. Examples include adenosine deaminase (*17*), guanine deaminase (*18*), cytosine deaminase (*11*), and SAH deaminase (*19*). The two notable exceptions are HutI and HutF. The structure of HutI from *B. subtilis* (*Bs*-HutI) has been determined in the presence of imidazole-4-acetic acid, an inhibitor that remotely resembles the substrate (*8*). From this HutI−ligand complex, a mechanism that utilizes the zinc in the active site to activate the hydrolytic water/hydroxide and a semiconserved glutamate at the end of β-strand 5 to facilitate proton transfer reactions has been proposed. Herein, we report three-dimensional X-ray structures of HutI from *A. tumefaciens* (*At*-HutI) and an environmental sample from the Sargasso Sea Ocean Going Survey (*Es*-HutI) bound to the product [*N*-formimino-L-glutamate (NIG)] and an inhibitor [3-(2,5-dioxoimidazolidin-4-yl)propionic acid (DIP) (also known as 3-ureidopropionate)], respectively (Figure 2). From these protein−ligand structures, an enzyme mechanism for the conversion of imidazolone-5-propionate to *N*-formimino-L-glutamate by HutI has been proposed.

EXPERIMENTAL PROCEDURES

Protein Production for At-HutI and Es-HutI. The *At*-HutI gene was amplified using polymerase chain reaction (PCR) from *A. tumefaciens* genomic DNA using a forward (CCAGGGAACAATTCTGCGAAGG) and a reverse (CTGGAGAAACCTTCTGTCCCTTG) primer. For *Es*-HutI, PCR from a Sargasso Sea environmental sample codon optimized synthetic gene using a forward (AATTGCGAACGTGTGTGGCTGAAC) and a reverse (CCCCATGCAGTGTTTCTTCACCG) primer resulted the final target gene. The amplified genes were gel purified and cloned into the pSGX3(BC) vector designed to express the protein of interest with a C-terminal hexahistidine affinity tag. Protein expression and purification utilized previously published protocols (*20*).

Preparation of Protein−Ligand Complexes. The apoenzyme crystals for *Es*-HutI and *At*-HutI were obtained in the $P3_221$ and $C2$ space group via sitting drop vapor diffusion at 20 °C against a reservoir solution containing 1.8 M triammonium citrate (pH 7.0) and 25% (w/v) PEG 3350, 0.1 M Bis-Tris (pH 5.5), and 0.2 M $MgCl_2$, respectively. The *Es*-HutI apo crystals were used for the inhibitor 3-(2,5-dioxoimidazolidin-4-yl)propionic acid (DIP) soaking experiments. The crystals were soaked in various concentrations of DIP (2, 3, 5, 8, and 10 mM) in reservoir solution [1.8 M triammonium citrate (pH 7.0)] and incubated for various time intervals ranging from 10 min to 12 h. The product, *N*-formimino-L-glutamate (NIG), was cocrystallized with *At*-HutI via hanging drop vapor diffusion at 20 °C against a reservoir solution containing 25% (w/v) PEG 3350, 0.1 M Bis-Tris (pH 5.5), and 0.2 M $MgCl_2$ (2 μL of protein at 30 mg/mL and 2 μL of reservoir solution). The protein solution contained six different protein:product molar ratios ranging from 1:1 to 1:6.

Data Collection, Structure Determination, and Refinement. Crystals soaked in 10 mM inhibitor for 12 h or produced via cocrystallization with a 1:3 protein:product molar ratio were flash-frozen by direct immersion in liquid nitrogen following cryoprotection with addition of 20% glycerol to the crystallization reservoir solution. High-resolution diffraction data (enzyme−inhibitor complex, 1.97 Å; enzyme−product complex, 1.83 Å) were recorded under standard cryogenic conditions using NSLS beamline X12C (National Synchrotron Light Source, Brookhaven National Laboratory), and diffraction data were processed using HKL2000 (*21*). Molecular replacement using the native model (PDB entry 2OOF) yielded the starting model for the inhibitor-bound structure and was refined using CNS (*22*). The product-bound structure was phased and refined using the native structure (PDB entry 2GOK) in CNS (*22*).

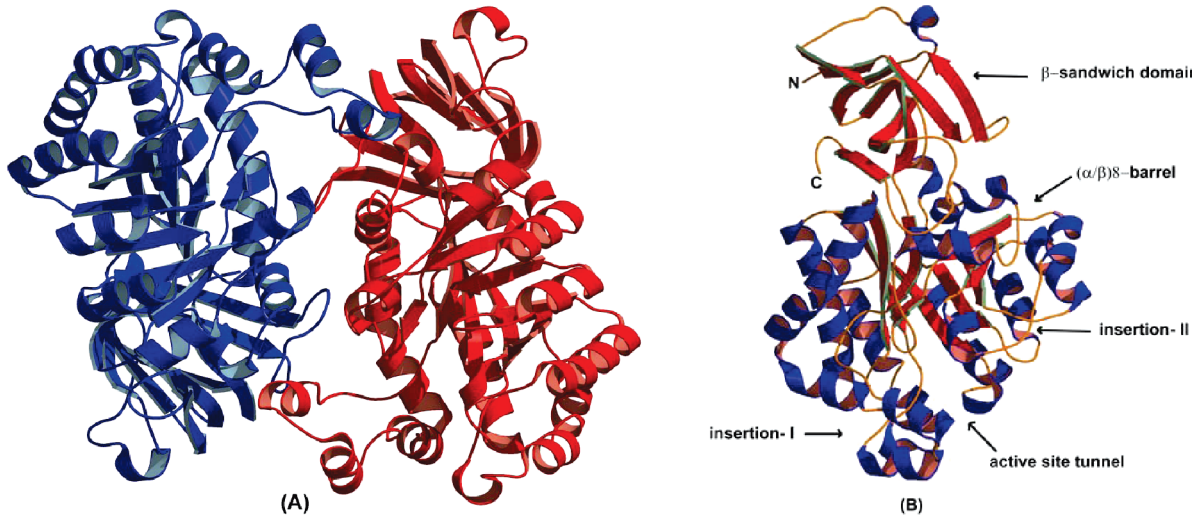

FIGURE 3: (A) Structure of the 2PUZ dimer. (B) Overall monomer structures of 2Q09 and 2PUZ, showing secondary structure elements.

Table 1: Data and Refinement Statistics

	product bound (2PUZ)	inhibitor bound (2Q09)
cell dimensions	a = 140.9 Å, b = 64.4 Å, c = 103.9 Å, β = 112.3°	a = 95.9 Å, b = 95.9 Å, c = 115.5 Å, γ = 120.0°
space group	$C2$	$P3_221$
Data Collection Statistics		
wavelength (Å)	1.1	1.1
temperature (K)	100	100
resolution range (Å)	50.0−1.83	50−1.97
no. of unique reflections	75466 (7337)[a]	42964 (3562)[a]
completeness (%)	99.5 (97.4)[a]	97.2 (81.6)[a]
mean $I/\sigma(I)$	27.9 (2.1)[a]	19.7 (1.9)[a]
redundancy	6.9 (5.7)[a]	17.6 (5.8)[a]
R_{merge}[b]	0.041 (0.169)[a]	0.063 (0.391)[a]
Refinement Statistics		
no. of reflections (work)	74509	41444
no. of reflections (test)	3784	1251
R_{factor}[c]/R_{free}[d]	0.198/0.225	0.194/0.214
resolution range (Å)	30.0−1.83	31.0−1.97
rmsd for bond lengths (Å)	0.005	0.006
rmsd for bond angles (deg)	1.30	1.4
$\langle B \rangle$ values		
main chain (Å^2)	29.8	30.8
side chain (Å^2)	31.2	32.4
no. non-hydrogen atoms		
heteroatoms	16	13
water molecules	587	275

[a] Values for the highest-resolution shell are given within parentheses. [b] $R_{merge} = \sum|I_i - \langle I \rangle|/\sum|I_i|$, where I_i is the intensity of the ith measurement and $\langle I \rangle$ is the mean intensity for that reflection. [c] $R_{factor} = \sum||F_{obs}| - |F_{calc}||/\sum|F_{obs}|$, where $|F_{calc}|$ and $|F_{obs}|$ are the calculated and observed structure factor amplitudes, respectively. [d] R_{free} equals R_{factor}, but for 5% of the total reflections chosen at random and omitted from refinement.

Difference Fourier syntheses revealed interpretable electron density features in the vicinity of the metal centers for 3-(2,5-dioxoimidazolidin-4-yl)propionic acid (DIP) and *N*-formimino-L-glutamate (NIG) in each cocrystal structure. During refinement, the stereochemical quality of both the models was monitored with PROCHECK (*23*). The final atomic coordinates and structure factors of both have been deposited with the Protein Data Bank (PDB entries 2Q09 and 2PUZ).

X-ray Fluorescence Scan and Inductively Coupled Plasma Mass Spectrometry Analyses. To identify the nature of the bound metal ion, fluorescence scanning for Zn, Fe, and Mg was performed with the protein solutions used for the crystallization before the data collection on beamline X12C (data not shown). The nature of the bound metal ion was also confirmed with inductively coupled plasma mass spectrometry (ICP-MS) analysis. Metal determination and quantification were performed with an Elan DRC II ICP-MS instrument from Perkin-Elmer. An analog detection mode was used with three averaged replicates per reading. External calibration standards were prepared through the serial dilution of a single 10 ppm stock mixture of Zn, Cd, Co, Cu, Mn, Ni, and Fe in 2% nitric acid. Freshly prepared standards generally contained 2, 20, and 200 ppb of the metal ions in 1% Trace Select nitric acid from Fluka, diluted in MilliQ deionized water. The masses of the isotopes detected were 55 for Mn, 57 for Fe, 59 for Co, 60 for Ni, 66 for Zn, and 111 for Cd. ^{115}In was used as an internal standard for ^{111}Cd, whereas ^{69}Ga was used as an internal standard for all other isotopes. The results showed the following metal content: 77% Fe, 10% Zn, and 13% Ni.

RESULTS AND DISCUSSION

Determination of the Structure of the Inhibitor-Bound Complex. The enzyme−inhibitor crystals belong to trigonal space group $P3_221$ (unit cell dimensions of a = 95.9 Å, b = 95.9 Å, c = 115.5 Å, and γ = 120°) with one complex per asymmetric unit, which is consistent with the protein monomer observed in solution via analytical gel filtration (data not shown). The atomic model was refined to a crystallographic R value of 19.4%, with an R_{free} of 21.4%. The stereochemistry of the model was of high quality as documented by PROCHECK (*23*), with ~90% of the residues found in the most favorable region of the Ramachandran plot. His265 and Asp23, both with well-defined electron density, adopt disallowed φ and ψ values. His265 is one of the active site residues. The final refined atomic model contains a single chain (residues 4−407) (Figure 3A), an iron molecule, and one DIP molecule, with 275 water molecules (Table 1).

Determination of the Structure of the Product-Bound Complex. The enzyme−product cocrystals belong to mono-

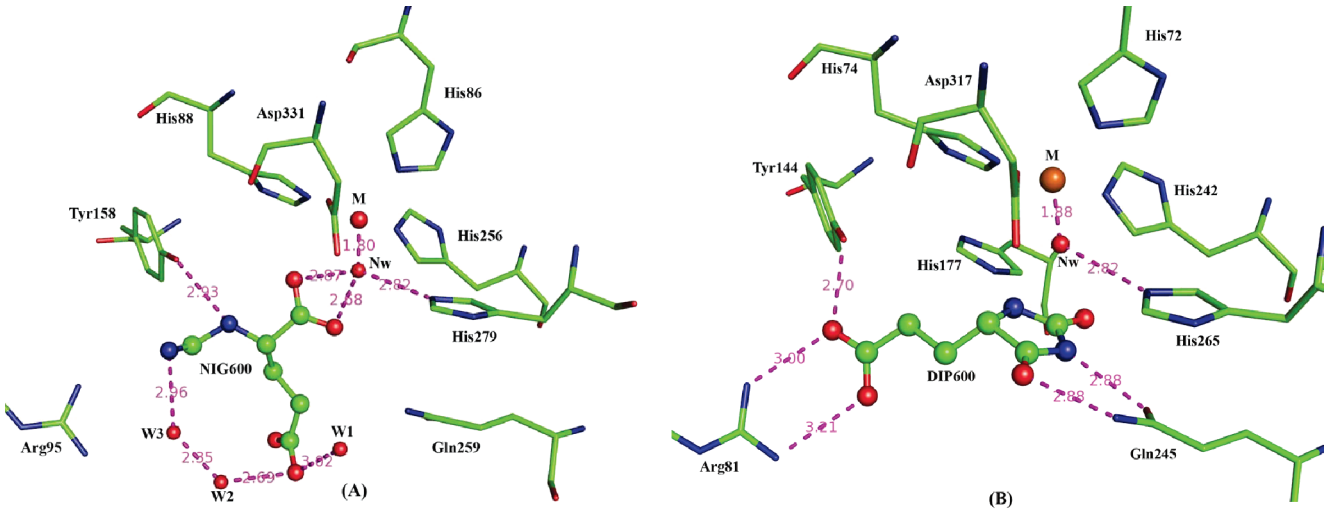

FIGURE 4: Active sites of the (A) enzyme−product and (B) enzyme−inhibitor complexes, shown in similar orientations. Nearby protein residues are shown as color-coded stick figures and ligand atoms as color-coded ball-and-stick figures (C, green; N, blue; O, red) with iron (M, orange) and water molecules (red) as spheres. Nw represents nucleophilic water, while W1−W3 represent structural waters stabilizing product binding.

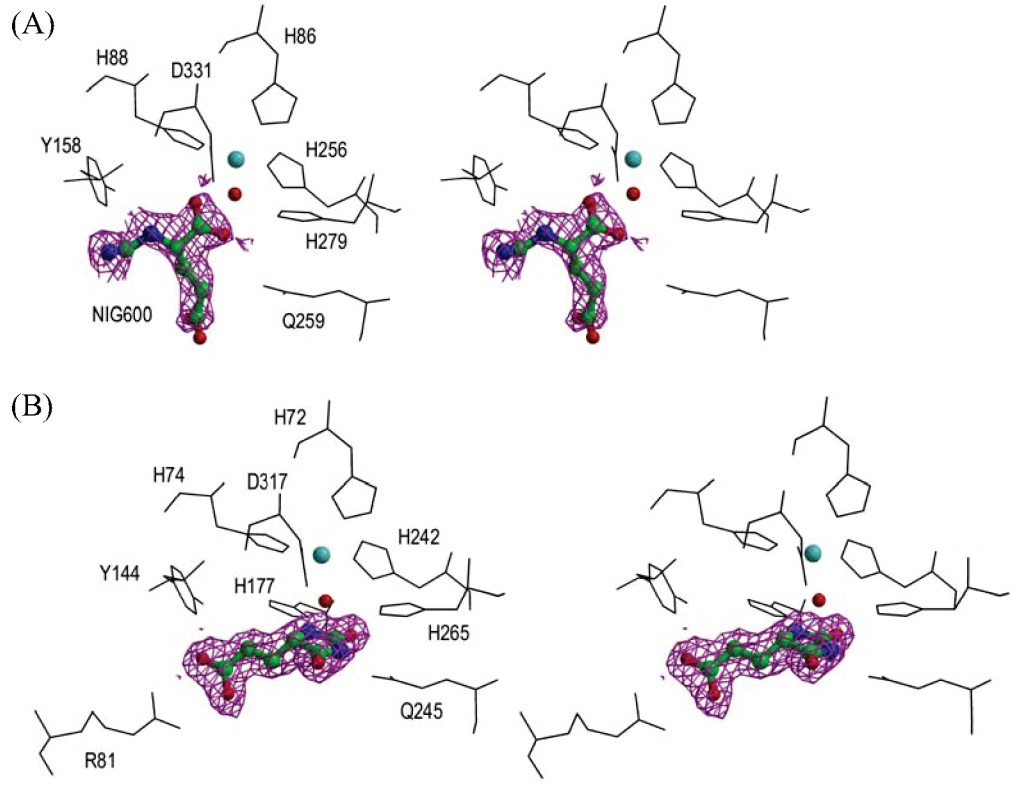

FIGURE 5: (A) Stereoview of the active site with the metal ion (cyan), the nucleophilic water (red), the bound product NIG, and (B) the inhibitor DIP. Both NIG and DIP are shown with their $2F_o - F_c$ electron density map contoured to the 1σ level.

clinic space group $C2$ (unit cell dimensions, $a = 140.9$ Å, $b = 64.4$ Å, $c = 103.9$ Å, and $\beta = 112.3°$) with two complexes per asymmetric unit. The atomic model was refined to a crystallographic R value of 19.8% with an R_{free} of 22.5%. The stereochemistry of the model was of high quality as documented by PROCHECK (*23*), with >90% of the residues found in the most favorable region of the Ramachandran plot. His279, with unambiguous electron density in both protomers, located in the active site at the C-terminus of a β-strand before a β-turn adopts disallowed φ and ψ values. The final refined atomic model contains two structurally similar polypeptide chains (residues 17−420) and two iron molecules, one magnesium (Mg^{2+}) cation, one chloride anion, and one NIG molecule, with 587 water molecules (Figure 3A and Table 1). The electron density for the NIG molecule was observed only in one monomer. The partially filled active site with the ligand is not uncommon. A root-mean-square deviation (rmsd) of 0.33 Å was calculated for 404 common α-carbon atomic pairs comprising the protein dimer. These two protomers are related by a noncrystallographic 2-fold axis, with each monomer burying ~1770 Å^2 of solvent accessible area upon dimerization, which exceeds values typically found in interacting surfaces for a protein of this size (*24*). However, this dimerization is an artifact of

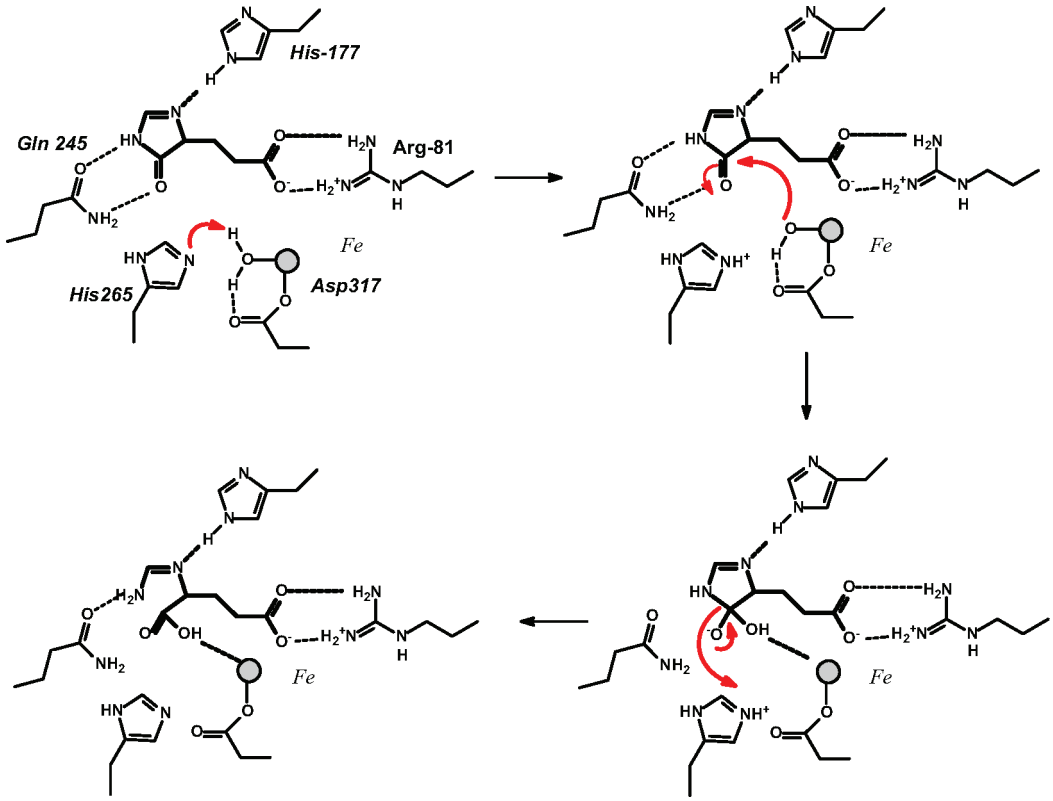

FIGURE 6: Reaction mechanism for HutI.

crystal packing as shown previously (*7*). At least 33 residues from each monomer are involved in dimer formation, with 12 direct hydrogen bonding interactions stabilizing the dimer interface.

Overall Structure of the Enzyme−Ligand Complexes. The overall monomer structures of both enzyme−ligand complexes are very similar with secondary structural compositions of ~20% β-strand, ~35% α-helix, and ~45% random coil. Each monomer is composed of a small β-sandwich N/C-terminal domain (*At*-HutI, residues 17−80 and 364−420; *Es*-HutI, residues 4−66 and 351−407) and a large middle domain, which adopts the $(\alpha/\beta)_8$-barrel characteristic of AHS (*At*-HutI, residues 81−379; *Es*-HutI, residues 67−365) (Figure 3B). The $(\alpha/\beta)_8$-barrel is interrupted twice by short segments of random coil and α-helix. Insert I is between residues 85 and 128 in *At*-HutI or between residues 71 and 114 in *Es*-HutI, which are inserted between strand β1 and helix α1, whereas insert II is between residues 301 and 316 in *At*-HutI or between residues 287 and 302 in *Es*-HutI between β7 and α7 (Figure 3B). These two insertions form the peptide flaps that border the entrance to the active site tunnel (barrel pore) at the C-terminal ends of its β-strands. A HINGEprot (*25*) analysis showed the role of two hinge residues (85 and 124 for *At*-HutI or 71 and 110 for *Es*-HutI) in opening and closing of this peptide flaps (*7*). The active site with its bound metal ion and ligands is located immediately behind these helical flaps. The $(\alpha/\beta)_8$-barrel fold is conserved among amidohydrolase superfamily members, and the overall structure of HutI has the highest degree of structural homology to cytosine deaminase (CDA) (*11*) with an overall rmsd among 353 α-carbon positions of 2.8 Å as reported by the DALI server (*26*). This structural similarity between enzymes with similar functions cannot be detected by BLAST searches due to the low degree of sequence identity between CDA and HutI (18%) or through available fold recognition servers, however, Holm and Sander had previously predicted on the basis of functional similarities and the evolutionary relationship in the aminohydrolase superfamily (*9*). It has been shown previously that the β-strands of the $(\alpha/\beta)_8$-barrel and the metal-binding residues of the active site correspond closely (rmsd = 0.3 Å for five metal-coordinating residues), whereas the external helices of the barrel and surface-exposed loops diverge significantly (*7*). The β-sandwich domain lies at the end of the barrel away from the active site and is formed by two separate peptide segments (residues 17−80 and 364−420 in *At*-HutI and residues 4−66 and 351−407 in *Es*-HutI), derived from opposite ends of the HutI primary sequence flanking the $(\alpha/\beta)_8$-barrel-forming sequence. This small β-sandwich domain is connected to the barrel by two short peptide linkers: the first is a random coil (residues 80−82 for *At*-HutI and 66−88 for *Es*-HutI), while the second is a helix (residues 357−372 for *At*-HutI and 344−359 for *Es*-HutI).

Architecture of the Product- and Inhibitor-Bound Active Site. The HutI active site is located within the negatively charged cavity of the $(\alpha/\beta)_8$-barrel domain and contains a single bound iron in both the structures. The presence of iron was initially identified by X-ray fluorescence analysis performed at NSLS beamline X12C and confirmed via inductively coupled plasma mass spectrometry (ICP-MS) analysis. It is remarkable that the enzyme from *B. subtilis* (*Bs*-HutI) contains a zinc metal ion instead of iron (*8*). In our product-bound structure, the iron is directly coordinated by His86 ($N^{\epsilon 2}$, 2.12 Å), His88 ($N^{\epsilon 2}$, 2.3 Å), His256 ($N^{\epsilon 2}$, 2.4 Å), and Asp331 ($O^{\delta 1}$, 2.3 Å) and a water nucleophile (1183, 1.8 Å) (Figure 4A), and similar coordination was

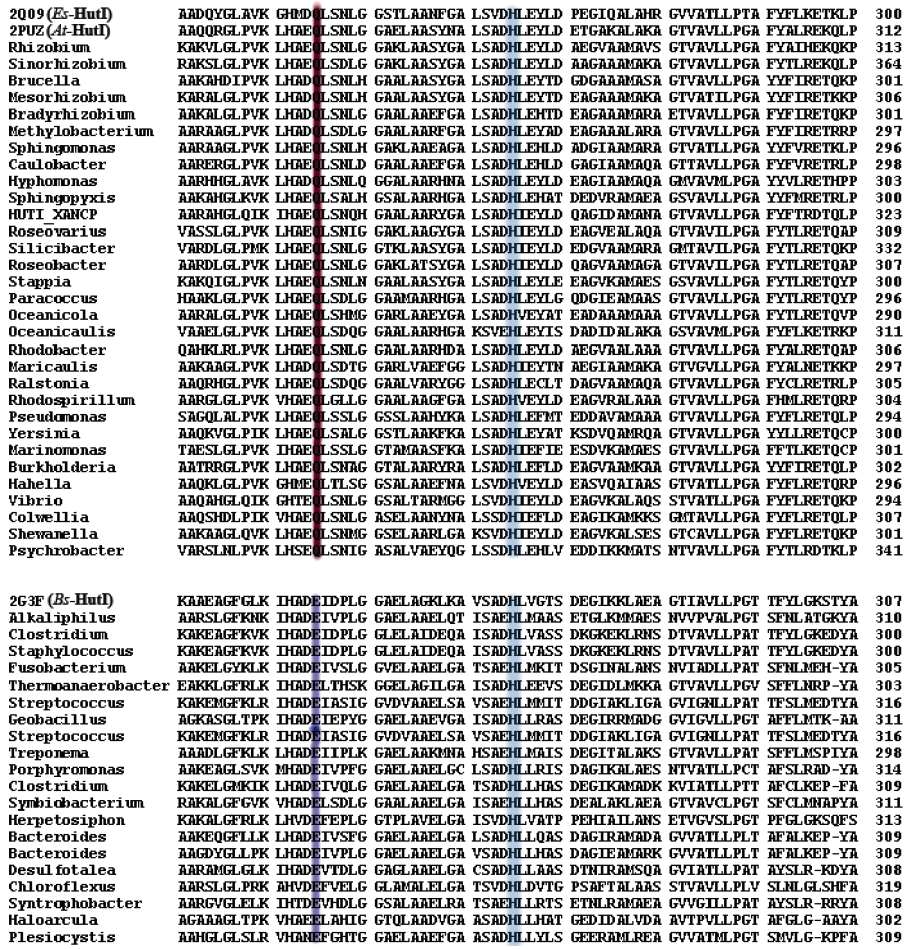

FIGURE 7: Multiple-sequence alignment of imidazolonepropionase sequences from various organisms showing two different classes of catalytic residues (Gln, red; Glu, blue) at positions 245 in *Es*-HutI (2Q09) or 259 in *At*-HutI (2PUZ) and 252 in *Bs*-HutI (2G3F). The conserved histdine (His265 in *Es*-HutI and His279 in *At*-HutI) is highlighted in sky blue.

observed in the inhibitor-bound complex with slight variations in metal ion coordination distances (His72, $N^{\epsilon 2}$, 2.1 Å; His74, $N^{\epsilon 2}$, 2.1 Å; His242, $N^{\epsilon 2}$, 2.3 Å; and Asp317, $O^{\delta 1}$, 2.3 Å) and a water nucleophile (260, 1.8Å) (Figure 4B). His279 in the product complex and His265 in the inhibitor complex both interact with the nucleophilic water (ion-side chain separation of ~2.8 Å). The catalytic metal ion and all surrounding side chains are well-ordered in the electron density maps.

Unbiased Fourier difference syntheses calculated with diffraction data from product-cocrystallized and inhibitor-soaked crystals display clear electron density for the bound product or inhibitor in the proximity of the $(\alpha/\beta)_8$-barrel (Figure 5A,B). Both electron density maps were calculated prior to the inclusion of ligands in the crystallographic model. The O^1 and O^2 atoms of the product NIG600 are 3.3 and 3.9 Å from the iron, respectively. The product also interacts with His88, Tyr158, nucleophilic water 1183, and waters W3 and W2 (Figure 4A). The N^1 atom of the inhibitor DIP600 is 4.9 Å from the iron and is slightly farther from it than the product (Figure 4B). Inhibitor DIP600 makes salt bridges with Arg81. In addition, DIP600 interacts with Gln245 and Tyr144 (Figure 4B). His72/86, His74/88, and Arg81/95 are from the insertion I region; His242/256 and His265/279 are located at the C-terminus of β-strands 5 and 6, respectively, and Tyr144/158, Gln245/259, and Asp317/331 are located in $\beta-\alpha$-loops 2, 5, and 8, respectively. Insertion I acts as a flap on the entrance of the central cavity (Figure 3B), making the metal ion and substrate binding site deeply buried in the molecule. The two cocrystal structures superimpose well in most of the regions, except between the flap region from insertion I (Ala96−Lys114, *At*-HutI numbering).

Mechanism of Action. The structures of HutI bound to product and an inhibitor in the active site enable a chemical reaction mechanism for this enzyme to be proposed. In this regard, the structure of HutI from the Sargasso Sea with bound inhibitor is more useful than the complex of HutI from *A. tumefaciens* with product. It appears that the complex of the product shows the product as it begins to depart from the active site. Thus, a water has now entered the coordination environment of the metal ion, the carboxylate group of the original substrate is no longer ion-paired with Arg95/Arg81, and the *N*-formimino group has rotated away from the initial cleavage site and appears H-bonded with Tyr158/Tyr144. The proposed reaction mechanism presented in Figure 6 is based on the inhibitor-bound structure. In the apoprotein active site, the lone metal ion is ligated to the protein via electrostatic interactions involving His72, His74, His242, and Asp317. The fifth ligand to the metal is a water/hydroxide molecule that is in turn hydrogen bonded to the side chain carboxylate group of Asp317 and the side chain imidazole of His265, which is conserved in all HutI forms (Figure 7). An identical set of ligands with the same geometry

is observed in the active sites of adenosine deaminase (*16*), guanine deaminase (*18*), cytosine deaminase (*9, 11, 26*), and SIH deaminase (*19*).

When substrate binds to the active site, the carboxylate functional group forms an ion pair with the side chain of invariant Arg81. The nitrogen attached to the α-carbon of the substrate forms a hydrogen bond to His177, and the carbonyl oxygen of the bond to be hydrolyzed forms a hydrogen bond to the carboxamide group of Gln245 and possibly with Thr322. These hydrogen bonding interactions serve to activate the carbonyl group for nucleophilic attack. There is no evidence in HutI, or in any of the other α-mononuclear metal-activated enzymes from the amidohydrolase superfamily, that the metal functions to polarize the carbonyl group (*10*). Catalysis is initiated by the transfer of a proton from the metal-bound water molecule to His265. The carbonyl carbon of the substrate is attacked by the metal-bound hydroxide to form a tetrahedral intermediate that is stabilized by the hydrogen bonding interactions with Gln245. This intermediate then collapses, and the product forms via the transfer of a proton from the charged His265 to the terminal nitrogen of the product.

Alternatives to the mechanism presented in Figure 6 can also be drawn. For example, a second proton transfer could occur from the metal-bound water/hydroxide to the side chain carboxylate of Asp317. This acid could then transfer this proton to the leaving group nitrogen upon collapse of the tetrahedral intermediate. In the reaction catalyzed by dihydroorotase, a member of the amidohydrolase superfamily with a binuclear metal center, there is excellent structural evidence for participation of the equivalent aspartate carboxylate group in the transfer of a proton from the bridging hydroxide to the leaving group nitrogen (*12*). In addition, a catalytic mechanism in which the final proton transfer is initiated by His177 for transfer to the nitrogen attached to the α-carbon can be devised. In this alternative mechanism, a different tautomer of the product would be formed and His177 would have to be initially protonated rather than neutral.

The mechanism proposed here for the hydrolysis of imidazole-5-propionate by HutI differs from that proposed earlier for HutI from *B. subtilis* (*8*). In the *B. subtilis* enzyme, the residue equivalent to Gln245 is a glutamate (Figure 7). Yu et al. have postulated that the leaving group nitrogen is protonated from this glutamate residue (Glu252) and that the other nitrogen is also protonated by a group that is ambiguously suggested as being the equivalent to His177 (His185). The mechanism of Yu et al. suggests no role for the fully conserved residue equivalent to His265 (His272) (Figure 7). We believe that the mechanism proposed by Yu et al. cannot be applied to any of the variants of HutI bearing a glutamine residue at the position equivalent to Gln245 from *Es*-HutI, since a glutamine is quite unlikely to support proton transfer as depicted for *Bs*-HutI (Figure 7). However, all of the variants mentioned in Figure 1 that have a glutamate at this position could operate by the mechanism proposed here for *At*-HutI and *Es*-HutI. A protonated glutamic acid could polarize the carbonyl group of the substrate and stabilize the tetrahedral adduct upon nucleophilic attack by the metal-borne hydroxide.

ACKNOWLEDGMENT

We gratefully acknowledge data collection support from beamline X12C (NSLS). We thank Robert Hall for the metal analysis.

REFERENCES

1. Borek, B. A., and Waelsch, H. (1953) The enzymatic degradation of histidine. *J. Biol. Chem. 205*, 459–474.
2. Magasanik, B., and Bowser, H. R. (1955) The degradation of histidine by *Aerobacter aerogenes*. *J. Biol. Chem. 213*, 571–580.
3. Schwede, T. F., Retey, J., and Shultz, G. E. (1999) Crystal Structure of Histidine Ammonia-Lyase Revealing a Novel Polypeptide Modification as the Catalytic Electrophile. *Biochemistry 38*, 5355–5361.
4. Kessler, D., Rétey, J., and Schulz, G. E. (2004) Structure and Action of Urocanase. *J. Mol. Biol. 342*, 183–194.
5. Schubert, C., Rottele, H., Spraul, M., and Retey, J. (1995) On the mechanism of action of urocanase: Observation of the enzyme-bound NAD^+-inhibitor adduct by ^{13}C NMR spectroscopy. *Angew. Chem., Int. Ed. 34*, 652–654.
6. Schubert, C., Zhao, Y., Shin, H.-H., and Retey, J. (1994) On the mechanism of the urocanase reaction: Cofirmation of the structure of the NAD^+-inhibitor adduct by direct ^{13}C-^{13}C coupling. *Angew. Chem., Int. Ed. 33*, 1279–1280.
7. Tyagi, R., Kumaran, D., Burley, S. K., and Swaminathan, S. (2007) X-ray structure of imidazolonepropionase from *Agrobacterium tumefaciens* at 1.87 Å resolution. *Proteins 69*, 652–658.
8. Yu, Y., Liang, Y.-H., Brostromer, E., Quan, J.-M., Panjikar, S., Dong, Y.-H., and Su, X.-D. (2006) A Catalytic Mechanism Revealed by the Crystal Structures of the Imidazolonepropionase from *Bacillus subtilis*. *J. Biol. Chem. 281*, 36929–36936.
9. Holm, L., and Sander, C. (1997) An evolutionary treasure: Unification of a broad set of amidohydrolases related to urease. *Proteins 281*, 72–82.
10. Seibert, C. M., and Raushel, F. M. (2005) Structural and catalytic diversity within the amidohydrolase superfamily. *Biochemistry 44*, 6383–6391.
11. Ireton, G. C., McDermott, G., Black, M. E., and Stoddard, B. L. (2002) The structure of *Escherichia coli* Cytosine Deaminase. *J. Mol. Biol. 315*, 687–697.
12. Porter, T. N., Li, Y., and Raushel, F. M. (2004) Mechanism for the Dihydroorotase Reaction. *Biochemistry 43*, 16285–16292.
13. Marti-Arbona, R., Fresquet, V., Thoden, J. B., Davis, M. L., Holden, H. M., and Raushel, F. M. (2005) Mechanism of the Reaction Catalyzed by Isoaspartyl Dipeptidase from *Escherichia coli*. *Biochemistry 44*, 7115–7124.
14. Marti-Arbona, R., and Raushel, F. M. (2006) Mechanistic Characterization of *N*-Formimino-L-Glutamate Iminohydrolase from *Pseudomonas aeruginosa*. *Biochemistry 45*, 14256–14262.
15. Hall, R. S., Xiang, D. F., Xu, C., and Raushel, F. M. (2007) *N*-Acetyl-D-glucosamine-6-phosphate Deacetylase: Substrate Activation via a Single Divalent Metal Ion. *Biochemistry 46*, 7942–7952.
16. Williams, L., Nguyen, T., Li, Y., Porter, T. N., and Raushel, F. M. (2006) Uronate Isomerase: A Nonhydrolytic Member of the Amidohydrolase Superfamily with an Ambivalent Requirement for a Divalent Metal Ion. *Biochemistry 45*, 7453–7462.
17. Wilson, D. K., Rudolph, F. B., and Quiocho, F. A. (1991) Atomic Structure of Adenosine Deaminase Complexed with a Transition State Analog: Understanding Catalysis and Immunodeficiency Mutations. *Science 252*, 1278–1284.
18. Liaw, S. H., Chang, Y. J., Lai, C. T., Chang, H. C., and Chang, G. G. (2004) Crystal Structure of *Bacillus subtilis* Guanine Deaminase. The first domain-swapped structure in the cytidine deaminase superfamily. *J. Biol. Chem. 279*, 35479–35485.
19. Hermann, J., Marti-Arbona, R., Fedorov, E., Fedorov, A., Almo, S., Shoichet, B. K., and Raushel, F. M. (2007) Structure-Based Activity Prediction for an Enzyme of Unknown Function. *Nature 448*, 775–779.
20. Rao, K. N., Bonanno, J. B., Burley, S. K., and Swaminathan, S. (2006) Crystal Structure of Glycerophosphodiester Phosphodiesterase from *Agrobacterium tumefaciens* by SAD with a Large Asymmetric Unit. *Proteins 65*, 514–518.
21. Otwinowski, Z., and Minor, W. (1997) Processing of X-ray Diffraction Data Collected in Oscillation Mode. *Methods Enzymol. 276*, 307–648.

22. Brunger, A. T., Adams, P. D., Clore, G. M., DeLano, W. L., Gros, P., Grosse-Kunstleve, R. W., Jiang, J. S., Kuszewski, J., Nilges, M., Pannu, N. S., Read, R. J., Rice, L. M., Simonson, T., and Warren, G. L. (1998) Crystallography & NMR system: A new software suite for macromolecular structure determination. *Acta Crystallogr. D54*, 905–921.
23. Laskowski, R. A., MacArthur, M. W., Moss, D. S., and Thornton, J. M. (1993) PRO-CHECK: A program to check the stereochemical quality of protein structures. *J. Appl. Crystallogr. 26*, 283–291.
24. Jones, S., and Thornton, J. M. (1996) Principles of protein-protein interactions. *Proc. Natl. Acad. Sci. U.S.A. 93*, 13–20.
25. HingeProt, http://bioinfo3d.cs.tau.ac.il/HingeProt/index.html.
26. Holm, L., and Sander, C. (1993) Protein structure comparison by alignment of distance matrices. *J. Mol. Biol. 233*, 123–138.

BI800180G